

# Uncertainty-Aware Lung Nodule Segmentation with Multiple Annotations

Qiuli Wang, Han Yang, Lu Shen, Mengke Zhang

**Abstract**—Since radiologists have different training and clinical experience, they may provide various segmentation maps for a lung nodule. As a result, for a specific lung nodule, some regions have a higher chance of causing segmentation uncertainty, which brings difficulty for lung nodule segmentation with multiple annotations. To address this problem, this paper proposes an Uncertainty-Aware Segmentation Network (UAS-Net) based on multi-branch U-Net, which can learn the valuable visual features from the regions that may cause segmentation uncertainty and contribute to a better segmentation result. Meanwhile, this network can provide a Multi-Confidence Mask (MCM) simultaneously, pointing out regions with different segmentation uncertainty levels. We introduce a Feature-Aware Concatenation structure for different learning targets and let each branch have a specific learning preference. Moreover, a joint adversarial learning process is also adopted to help learn discriminative features of complex structures. Experimental results show that our method can predict the reasonable regions with higher uncertainty and improve lung nodule segmentation performance in LIDC-IDRI.

**Index Terms**—Lung Nodule, Segmentation, Uncertainty, Semantic Feature

## I. INTRODUCTION

Lung nodule segmentation with multiple annotations is a task closely related to the clinical diagnosis process and plays a crucial role in Computer-Aided Diagnosis (CAD) systems for lung nodule [1]. Traditional methods usually ignore the uncertain regions between multiple annotations and select a single annotation as the learning target [2]–[5]. To make the most of multiple annotations, studies like [6]–[8] propose to model these uncertainties as probabilistic distributions and produce segmentation masks with the random variables in latent space. However, relying on random variables, these methods cannot produce stable segmentation maps. How to make full use of multiple annotations is a problem that remains to be solved.

In this paper, we propose that regions that cause uncertain segmentation results are not ‘random’, and some features have higher chances that cause uncertainty between multiple annotations. More importantly, conventional deep learning methods also have difficulty in dealing with these regions and features. To demonstrate our findings, we propose to fuse all annotations for a lung nodule as the Multi-Confidence Mask (MCM). As shown in Figure 1.A, the MCM is the combination of the multiple annotations’ union and intersection. We define two categories for the mask pixels: High Confidence (HC) mask and Low Confidence (LC) mask. The HC mask is the region labeled by all radiologists (intersection of all annotations),

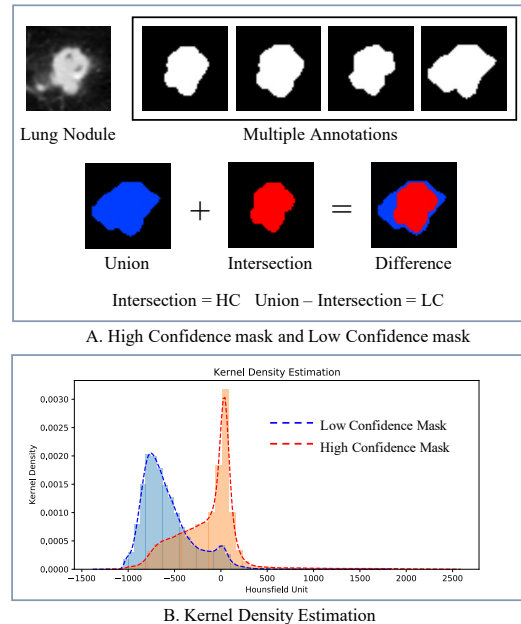


Fig. 1: A: Overview of High Certainty (HC) mask, Low Certainty (LC) mask, and Multi-Confidence Mask. B: Kernel density estimation of HC and LC masks in LIDC-IDRI. The HU in LC are mainly distributed around  $HU -750$ , and the HU in HC are mainly distributed around  $HU 0$ . The MCM is combined with HC and LC masks.

and the LC mask is the region that the radiologists have disagreements (the difference of union and intersection). **The question is, what causes the differences between HC and LC masks?**

To reveal this phenomenon, we further calculate the HU (Hounsfield Unit) kernel estimations in HC and LC of LIDC-IDRI [9], and show them in Figure 1.B. As can be seen, HC and LC masks have quite different HU distributions: HU values in HC masks are mainly distributed around  $HU 0$ , while HU values in LC masks are mainly distributed around  $HU -750$ . This phenomenon indicates that the radiologists may have more diverse opinions about nodule low dense tissues and boundaries [10]. This study’s goal is to learn the HC and LC according to their density characteristics, ensure the segmentation performance of HC regions, and improve the segmentation performance of LC regions as well as possible. By doing so, we can improve the overall segmentation performance, and predict lung nodule regions with different segmentation uncertainties.

To achieve this goal, we introduce a Uncertainty-Aware Segmentation Network (UAS-Net). This network is based

on a multi-branch U-Net, and each branch has a specific learning target: one for the annotations' union, one for the annotations' intersection, and one for the single plausible annotation between the union and intersection. The learning of union and intersection can be combined as the predicted MCM, and all targets contribute to the final segmentation result.

The main challenge for our UAS-Net is to learn the discriminative visual features from different learning targets, especially these regions with different segmentation uncertainties. we address this challenge by introducing a Feature-Aware Concatenation (FA-Cat) that can control the learning preferences. The FA-Cat first uses the self-attention mechanism to compress feature maps, then uses a replaceable self-adaptive method to capture specific visual features for the concatenation. The self-adaptive method decides the learning preferences of FA-Cat, the self-attention mechanism help to resolve more features after feature map compression, and by switching the self-adaptive method, we can adjust the learning preference of each branch.

Moreover, we introduce a joint adversarial process to guide the parameters' training, which contains a lung nodule synthesis network and a malignancy level discriminator. The synthesis network guides the learning of the uncertain region features by transforming the MCM masks to images, since the better mask can contribute to better synthesis results [11], [12]. The a malignancy level discriminator is used to guide the learning of discriminative features jointly.

Our contributions can be summarized as follows: (1) We introduce a Multi-Confidence Mask (MCM), which can combine multiple annotations' union and intersection, and reflect lung nodule regions with different segmentation confidences. (2) We propose a Uncertainty-Aware Segmentation Network (UAS-Net), which aims to learn the valuable visual features from regions with different uncertainty levels, improve the segmentation performance, and provide MCM simultaneously. (3) We introduce a Feature-Aware Concatenation (FA-Cat). By combining the self-attention mechanism and self-adaptive method, FA-Cat can change learning preferences during concatenation.

## II. METHODS

### A. The Network Architecture

The architecture of the Uncertainty-Aware Segmentation Network is shown in Figure 2. The input of the network is a  $n$  - annotation set  $A = \{a_1, a_2, \dots, a_n\}, n \leq 4$ , where  $n$  represents the annotation number. Then the network has three learning targets: intersection  $\cap(A)$ , union  $\cup(A)$  and specific annotation  $R(A)$ . The  $\cap(A)$  indicates the regions that all radiologists' consensus; the  $\cup(A)$  shows the possible largest region of lung nodules; the  $\cup(A) - \cap(A)$  indicates the regions that may cause disagreements; the  $R(A)$  provides a possible result between the consensus and disagreements. The Multi-Confidence Mask (MCM) is the combination of  $\cup(A) - \cap(A)$  and  $\cap(A)$ . The selection of single annotation is consistent with studies [13], [14]. Since the area of  $\cup(A) - \cap(A)$  is too small for learning, we use the union set  $\cup(A)$  instead of

$\cup(A) - \cap(A)$  as the learning target. The learned union and intersection are combined directly as the MCM.

Sharing the same down-sampling process, our method has three up-sampling branches. The first branch is assigned for the learning of multiple annotations' union  $\cup(A)$ , the second branch is assigned for the learning of multiple annotations' intersection  $\cap(A)$ . The last branch is a general U-Net up-sampling branch. All branches are concatenated together for the learning of a specific annotation  $R(A')$ . Correspondingly, we have predicted  $\cup(A')$ ,  $\cap(A')$ , and  $R(A')$ .

The first two branches have specific learning preferences by using different adaptive methods of Feature-Aware Concatenation Block (FA-Cat), and the third branch obtains a conventional segmentation map by using the traditional encoding-decoding structure. The  $R(A')$  obtained by combining features captured by different branches is the segmentation result with the largest amount of information for each lung nodule, which is the overall segmentation. The details of FA-Cat will be discussed in Section II-B. Then, we fuse the  $\cup(A')$  and  $\cap(A')$  as Multi-Confidence Mask (MCM) to show different certainty levels of each lung nodule's different regions by adding the  $\cup(A')$  and  $\cap(A')$  directly:

$$MCM = \text{normalize}(\cup(A') + \cap(A')) \quad (1)$$

Moreover, we design a joint adversarial loss to guide the network: (1) It forces the network to generate a better MCM by transforming the mask back to nodule image using a pix2pix [15], [16], since better mask quality contributes to better nodule synthesis [17], [18]; (2) It guides all branches to learn discriminative features using a malignancy level discriminator.

### B. Feature-Aware Concatenation

The advantage of our network is that our network can use different concatenation strategies for a specific learning targets, which is achieved by introducing a Feature-Aware Concatenation. The architecture of FA-Cat is shown in Figure 3. Assuming the convolutional feature maps is  $\mathbf{X} \in \mathbb{R}^{c \times w \times h}$ , it will pass the FA-Cat and gets  $\mathbf{U} \in \mathbb{R}^{(c+\frac{c}{16}) \times w \times h}$ . The FA-Cat sequentially has two blocks: a Squeeze-and-Excitation (SE) Block, and a Squeeze-and-Adapt (SA) Block.

The SE Block is based on Spatial Squeeze and Channel Excitation Block (cSE) [19] and learns the channel-wise information of convolutional feature maps. First, we apply the global average pooling on  $\mathbf{X}$  and get a vector  $z \in \mathbb{R}^{c \times 1 \times 1}$ . Next  $z$  will be fed into an encoder-decoder operation defined as  $\tilde{z} = W_1(W_2z)$ , where  $W_1 \in \mathbb{R}^{C \times \frac{C}{16}}$ , and  $W_2 \in \mathbb{R}^{\frac{C}{16} \times C}$ . Then we have  $\tilde{z} \in \mathbb{R}^{c \times 1 \times 1}$ . Finally, we get the output  $\mathbf{U} = \mathbf{X} \times \tilde{z}$ ,  $\mathbf{U} \in \mathbb{R}^{c \times w \times h}$ .

The Squeeze-and-Adapt (SA) Block combines the original conventional features with the features learnt by the self-adaptive method. First, SA Block compresses the  $\mathbf{U} \in \mathbb{R}^{c \times w \times h}$  to  $\mathbf{U}' \in \mathbb{R}^{\frac{c}{16} \times w \times h}$ . Then the self-adaptive method  $\xi$  will extract visual features from  $\mathbf{U}'$  and gets  $\xi(\mathbf{U}') \in \mathbb{R}^{\frac{c}{16} \times w \times h}$ . The final output of SA Block which is also the output of FA-Cat is  $\mathbf{Y} = \mathbf{U} \oplus \xi(\mathbf{U}')$ ,  $\mathbf{Y} \in \mathbb{R}^{(c+\frac{c}{16}) \times w \times h}$ , where  $\mathbf{U}$  is the output of SE Block, and  $\xi(\mathbf{U}')$  provides features learnt by the self-adaptive method. In the two FA-Cats

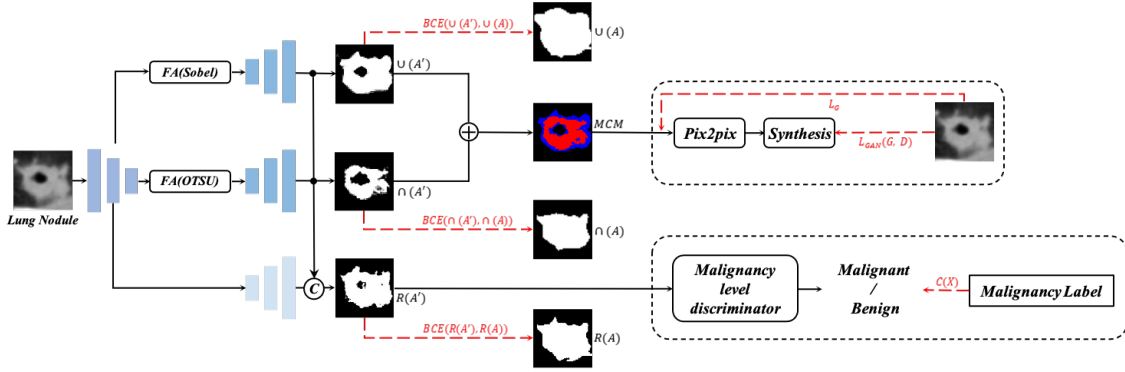


Fig. 2: Overview of the Uncertainty-Aware Segmentation Network. The network contains three up-sampling branches sharing the same down-sampling process. For the learning of multiple annotations' union and intersection, the first two branches adopt the Feature-Aware Concatenation (FA-Cat) which can change the learning preferences of by switching the adaptive methods during concatenation. We use a pix2pix for the better generation of the multi-confidence mask, and use a malignancy level discriminator for the better learning of discriminative visual features.

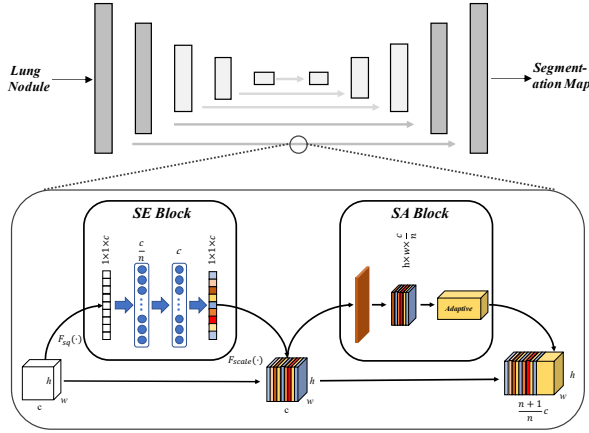


Fig. 3: Illustration for the FA-Cat. Our network contains five down-sampling layers, and each branch has five up-sampling layers. Each down-sampling and up-sampling layers are connected with concatenation correspondingly. The first two layers use our FA-Cat, and the last three layers use the general concatenation of U-Net.

of our network, we select Sobel edge detection and Otsu [20] respectively as adaptive methods to extract different features. The reason we choose these two methods is that: (1) The learning of intersection needs to pay more attention to the high-dense nodule regions. As mentioned in the study [11], Otsu can reserve the nodule density information well, so we adopt Otsu in the FA-Cat for the intersection learning; (2) The learning of union needs to pay more attention to the low-dense nodule regions. Otsu can reserve the low-dense regions well, but it cannot capture delicate features around the nodule, such as spiculation. In this case, the method which can capture texture information is better. As a result, we choose Sobel in the FA-Cat for the union learning.

### C. Loss Functions

First of all, we use BCE (Binary Cross-Entropy) to measure the segmentation loss:

$$S(A, A') = BCE(\cap(A'), \cap(A)) + BCE(\cup(A'), \cup(A)) + BCE(R(A'), R(A)) \quad (2)$$

Secondly, the Multi-Confidence Mask (MCM)  $M$  will be transformed back to lung nodule CT image  $X'$  with an adversarial pix2pix, which contains a generator and a discriminator. The loss for pix2pix generator is defined as  $\mathcal{L}_G$ :

$$\mathcal{L}_{L1}(G) = \mathbb{E}_{X, M, A} [\|A - G(X, M)\|_1] \quad (3)$$

where  $G$  is the pix2pix generator that transforms MCM  $M$  to synthesis CT image  $X'$  according to  $X$ . The pix2pix discriminator based on conventional CNN is used to discriminate the input tuples:  $\{X', M\}$  and  $\{X, M\}$ :

$$\mathcal{L}_{GAN}(G, D) = \mathbb{E}_{X, M} [\log D(X, M)] + \mathbb{E}_{X', M} [\log(1 - D(X', M))] \quad (4)$$

Moreover, a CNN discriminator  $C$  is used to discriminate the malignancy level of input  $R(A')$ , which also adopts the cross-entropy as the loss function.

Then we have our final object:

$$\arg \min_{G, S, C} \max_D \mathcal{L}_{GAN}(G, D) + \mathcal{L}_{L1}(G) + S(A, A') + C(R(A')) \quad (5)$$

## III. EXPERIMENTS

### A. Dataset and Experimental Settings

The used dataset is LIDC-IDRI [9], which has 2635 annotated lung nodules with malignancy labels. We extract 1859 lung nodules, and calculate the intersection and union of annotations through their multiple annotations. To comprehensively evaluate the network, we use five-cross validation in this study. We split the dataset into five folds and ensure each fold has the same malignant/benign nodule distributions. Our network is built on PyTorch [21]. All experiments are run on a GPU of NVIDIA Tesla V100.

### B. Performance of General Lung Nodule Segmentation

We use Dice and IoU as the evaluation metrics for the lung nodule segmentation, and compare our network with a variety of commonly used medical image segmentation networks which are trained with single annotation. The experimental

results are shown in Table I. According to Table I, the average dice score of our network is 85.04, which is the highest comparing to other methods. Generally speaking, U-Net-based methods have better performances than traditional machine learning methods. R2U-Net [22] achieves 83.59, which uses recurrent residual block to effectively increase the depth of the network and make the network could extract better features. The Channel U-Net [23] applies the channel-attention unit recursively on feature maps at every layer of the network, which is effective and it achieves 84.02. Our UAS-Net achieves 85.04, which is the highest. At the same time, our average IoU value is 73.94, which is better than all the above methods except the Multi-Orientation U-Net [24]. However, the Dice value of Multi-Orientation U-Net is only 83.00, so in general, the performance of our method is still convincing.

TABLE I: Comparison between our framework and existing methods on the LIDC-IDRI dataset. JA indicates the joint adversarial loss.

| Method                       | Dice         | IoU          |
|------------------------------|--------------|--------------|
| Level Set [25]               | 60.63        | -            |
| Graph Cut [13]               | 68.90        | -            |
| CF-CNN [13]                  | 82.15        | -            |
| FCN V-Net [26]               | 79.59        | -            |
| R2U-Net [22]                 | 83.59        | -            |
| Dual-branch ResNet [14]      | 82.74        | -            |
| Multi-Orientation U-Net [24] | 83.00        | 76.00        |
| 3D CNN [27]                  | 83.10        | 71.85        |
| Channel U-Net [23]           | 84.02        | 73.53        |
| Nested U-Net [28]            | 83.44        | 72.72        |
| Baseline(U-Net) [29]         | 83.54        | 73.19        |
| UAS-Net                      | <b>85.04</b> | <b>73.94</b> |

The key to performance improvements is that each branch can capture different visual features with the help of FA-Cat. As mentioned above, our network uses two versions of FA-Cat: one adopts the Sobel edge detection, another one adopts the Otsu. We expect that FA-Cat (Sobel) can pay more attention to the delicate features and help the learning of union, and FA-Cat (Otsu) can pay more attention to the density changes and the learning of intersection. To intuitively observe the effect of Fa-Cat, we visualize the activation heatmaps of conventional features in the last CNN layer of FA-Cat with Figure 4. As can be seen, the FA-Cat (Sobel) and FA-Cat (Otsu) have different learning interests, obviously. FA-Cat (Otsu) pays more attention (red) to high dense areas in lung nodules, while the FA-Cat (Sobel) pays more attention (yellow) to the lung nodules' edge. In Figure 4 we also show the 3D visualization of the most active neurons in the CNN layers with red pillars. It is quite clear that FA-Cat (Otsu) activates more neurons in the nodule centers while the FA-Cat (Sobel) activates more neurons around the nodules. It means FA-Cat (Sobel) and FA-Cat (Otsu) work as we expected.

By combining the multiple branches, our method can learn the features of high dense areas and edge areas simultaneously, contributing to better overall segmentation performance. In order to prove the above conclusion, we compare the segmentation results of different methods in Figure 5. As can be seen, our method has better performance when dealing with lung nodules with complex structures, such as low dense tissues.

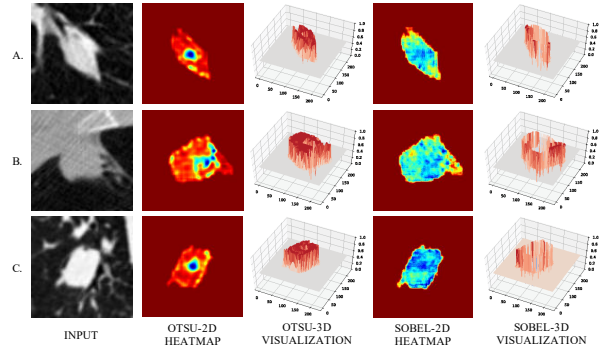


Fig. 4: Visualization of convolutional 2D and 3D activation heatmaps in FA-Cat (Sobel) and FA-Cat (Otsu). It can be seen that FA-Cat (Sobel) pays more attention to the edge of pulmonary nodules, while FA-Cat (Otsu) pays more attention to the high-density areas of pulmonary nodules.

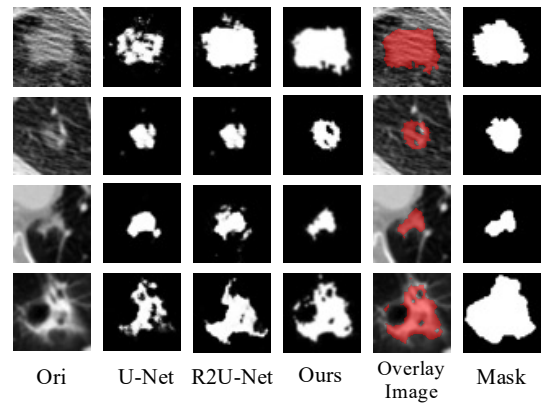


Fig. 5: Segmentation comparisons between U-Net, R2U-Net, and our method. It can be seen that the our method has a better segmentation effect on nodules with cavities, spiculation signs or low-density nodules.

### C. Prediction of the Multi-Confidence Mask

This section contains two parts. The first part discusses the prediction of union and intersection of the annotation set, which is the basis of the Multi-Confidence Mask. The second part demonstrates the prediction of the Multi-Confidence Mask.

1) *Multiple Annotations' Union and Intersection*: The quality of the predicted union and intersection directly affects the final estimation of Multi-Confidence Mask (MCM). To demonstrate the performance of union and intersection prediction, we design a comparative experiment of U-Net [29], Dual-Branch U-Net (which add a general branch to the original U-Net), Feature-Aware Dual-Branch U-Net (which add the Feature-Aware Concatenation Block to the Dual-Branch U-Net) and our method. The difference between our method and Feature-Aware Dual-Branch U-Net is that our method contains a joint adversarial learning process and one more branch for the final segmentation. The experimental results are shown in Table II.

According to the Table II, the original U-Net achieves an average Dice of 0.8361 with single annotation for each lung nodule. Meanwhile, U-Net achieves average Dice scores of 0.8337 and 0.8611 with annotation intersection and union.



TABLE II: Prediction of Intersection and Union

| Framework                        | Dice          |
|----------------------------------|---------------|
| <i>Normal Segmentation</i>       |               |
| U-Net                            | 0.8361        |
| <i>Intersection Segmentation</i> |               |
| U-Net                            | 0.8337        |
| Dual-Branch U-Net                | 0.8367        |
| Feature-Aware Dual-Branch U-Net  | 0.8395        |
| Our Method                       | <b>0.8403</b> |
| <i>Union Segmentation</i>        |               |
| U-Net                            | 0.8611        |
| Dual-Branch U-Net                | <b>0.8698</b> |
| Feature-Aware Dual-Branch U-Net  | 0.8535        |
| Our Method                       | 0.8689        |

Compared to the U-Net, Dual-Branch U-Net has similar performance in the intersection prediction, the Feature-Aware concatenation achieves 0.8395, and our network achieves the highest 0.8403. It means our Feature-Aware concatenation and the joint adversarial process can improve the intersection prediction. In the union prediction, Dual-Branch achieves the highest 0.8698, the Feature-Aware Dual-Branch U-Net achieves 0.8535, which is the lowest, and our network reaches 0.8689, which is higher than the U-Net, but slightly lower than Dual-Branch U-Net.

2) *Multi-Confidence Mask*: Figure 6 shows the segmentation of multiple annotations' union, intersection, and MCM. Colors are used to show the differences, and the original outputs are grayscale.

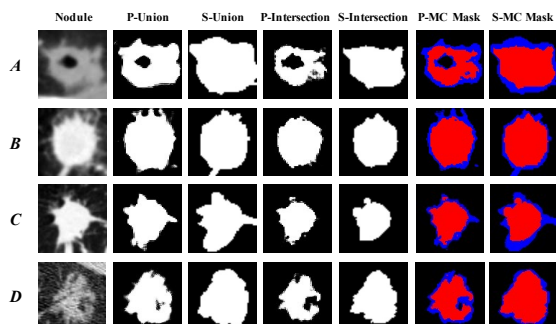


Fig. 6: Prediction of the Multi-Confidence Mask. For each nodule, we provide the predicted union (P-Union), the predicted intersection (P-Intersection), the predicted MCM (P-MC Mask), and the standard union (S-Union), intersection (S-Intersection), MCM (S-MC Mask). The blue regions in the MCM (standard/predicted) indicate the regions that have higher uncertainty.

As can be seen, our Multi-Confidence Mask (MCM) has several advantages: (1) MCM can better show the significant cavitory features of lung nodules (Figure 6 A). On the prediction of the intersection, the cavity is obviously larger, and we believe it is because the prediction is associated with density: the density of the lung nodule is smaller than the nodule core. (2) MCM can better show the spiculation sign, which is an important feature for the diagnosis of the malignant nodule (Figure 6 B, C). The spiculation is a stellate distortion caused by the intrusion of nodules into surrounding tissue [30], which is low-dense and distributed at the nodule edges. The network pays more attention to the low-dense tissues when segmenting the union of multiple annotations. As a result, it naturally

has better performance on spiculation sign segmentation. (3) MCM can segment the part-solid nodule (Figure 6 D) better, which means the network can take advantage of the multiple annotations since the experts tend to have different opinions in the low-dense regions.

Since the LC and HC masks are small and Dice can not directly measure the ability of MCM prediction, we calculate the HU distributions in HC and LC masks, and compare them with the real ones. If our network can predict the regions with high uncertainty well, the HU distributions of predicted HC and LC should also fit the same distribution. As shown in this Figure 7, the predicted and real curves are almost the same, which means our predicted uncertain regions are convincing from the perspective of statistics.

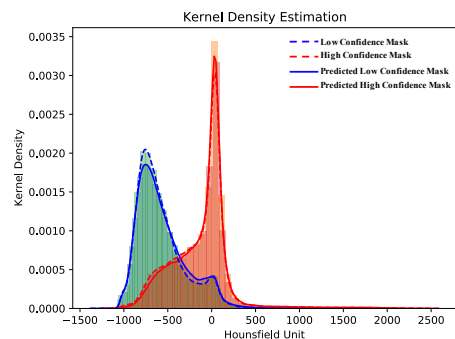


Fig. 7: Kernel density estimation for the predicted HC and LC. The dotted lines indicate the real annotations, and the solid lines mean predicted annotations. As can be seen, our prediction has a very similar kernel density estimation, which means they have almost the same data distribution.

#### D. Effect of the Joint Adversarial Process

To demonstrate the effect of the joint adversarial process, we perform two experiments, one contains JAP (Joint Adversarial Process), and one does not. The results of the five-fold evaluation are listed in Table III. As can be seen, the adversarial learning process leads to lower Dice scores in all five folds.

TABLE III: Dice of Five-Cross Validation

| Models             | Fold1  | Fold2  | Fold3  | Fold4  | Fold5  | Average       |
|--------------------|--------|--------|--------|--------|--------|---------------|
| Ours (without JAP) | 0.8470 | 0.8516 | 0.8546 | 0.8548 | 0.8563 | <b>0.8529</b> |
| Ours               | 0.8432 | 0.8503 | 0.8522 | 0.8532 | 0.8533 | <b>0.8504</b> |

As mentioned above, our adversarial learning process contains two parts: (1) A MCM to CT image transformation with  $\text{pix}2\text{pix}$ ; (2) A malignancy level discriminator. The transformation between MCM and CT image forces the network to pay more attention to the low texture tissues, which are low-dense, while the malignancy level discriminator helps the learning of spiculation. The Dice score drops because the adversarial learning forces the network to learn more delicate features such as cavities, spiculation, et. al.

To better demonstrate this phenomenon, we show six nodules with segmentations in Figure 8. We can clearly see that the network can extract more details (the red box in the figure) of spiculation, low texture level, and cavity with the adversarial

process. Nodule **A**, **B**, **C**, and **D** have cavities or low-dense tissues. The adversarial learning makes the gaps in the segmentation larger, which will decrease the Dice. Nodule **A**, **D**, and **E** have complete nodule edges such as spiculation. Our joint adversarial learning process also improves the detection of such features, which will also decrease the Dice. Meanwhile, a large part of this Nodule **F** is low-dense. Our joint adversarial learning helps to segment more nodule tissues. However, cases like this one are rare, and they will not improve the average Dice.

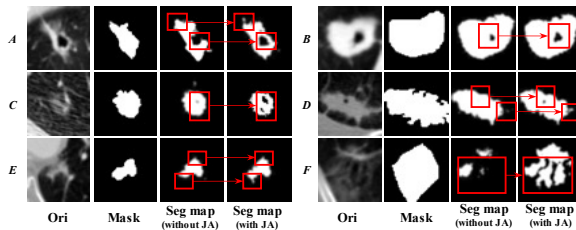


Fig. 8: Effect of joint adversarial process. Red blocks show that joint adversarial learning can improve the segmentation of the spiculation, cavity, and part-solid nodules. ‘JA’ means ‘Joint Adversarial Learning’.

In summary, with the joint adversarial learning, the network can capture more minor features of nodules which aren’t marked by standard mask. Although the segmentation of this feature will lead to a slight decrease in Dice, these features can provide valuable information for the diagnoses of malignant lung nodule. Therefore, we believe the joint adversarial process is of value.

#### IV. CONCLUSIONS

This paper proposes a Uncertainty-Aware Segmentation Network, which can learn from the diverse annotations for each lung nodule and improve overall segmentation performance simultaneously. The network contains three up-sampling branches that sharing the same down-sampling process for three targets. By calculating the difference of the learned intersection and union, the network show nodule regions with different certainty level with the Multi-Confidence Mask. All three branches together produce one plausible segmentation between the consensus and disagreements. We evaluate our network on LIDC-IDRI. Experimental results show that our method can predict lung nodule regions with high uncertainty levels and provide better segmentation.

#### REFERENCES

- [1] H. Liu, H. Cao, E. Song, and *et al.*, “A cascaded dual-pathway residual network for lung nodule segmentation in ct images,” *PHYS MEDICA*, vol. 63, pp. 112–121, 2019.
- [2] W. Zhu, C. Liu, W. Fan, and *et al.*, “Deeplung: Deep 3d dual path nets for automated pulmonary nodule detection and classification,” in *Proc. IEEE WACV*, 2018, pp. 673–681.
- [3] H. Xie, D. Yang, N. Sun, and *et al.*, “Automated pulmonary nodule detection in ct images using deep convolutional neural networks,” *PATTERN RECOGN*, vol. 85, pp. 109–119, 2019.
- [4] L. Gonçalves, J. Novo, and A. Campilho, “Hessian based approaches for 3d lung nodule segmentation,” *EXPERT SYST APPL*, vol. 61, pp. 1–15, 2016.
- [5] D. Wu, L. Lu, J. Bi, and *et al.*, “Stratified learning of local anatomical context for lung nodules in ct images,” in *Proc. IEEE CVPR*, 2010, pp. 2791–2798.
- [6] S. Kohl, B. Romera-Paredes, C. Meyer, and *et al.*, “A probabilistic u-net for segmentation of ambiguous images,” in *Proc. NIPS*, 2018, pp. 6965–6975.
- [7] S. Hu, D. Worrall, S. Knecht, and *et al.*, “Supervised uncertainty quantification for segmentation with multiple annotations,” in *Proc. MICCAI*. Springer, 2019, pp. 137–145.
- [8] S. A. Kohl, B. Romera-Paredes, K. H. Maier-Hein, and *et al.*, “A hierarchical probabilistic u-net for modeling multi-scale ambiguities,” *arXiv preprint arXiv:1905.13077*, 2019.
- [9] S. Armato III, G. McLennan, L. Bidaut, and *et al.*, “The lung image database consortium (lidc) and image database resource initiative (idri): a completed reference database of lung nodules on ct scans,” *MED PHYS*, vol. 38, no. 2, pp. 915–931, 2011.
- [10] M. Gao, U. Bagci, L. Lu, and *et al.*, “Holistic classification of ct attenuation patterns for interstitial lung diseases via deep convolutional neural networks,” *Comput Methods Biomech Biomed Eng Imaging Vis*, vol. 6, no. 1, pp. 1–6, 2015.
- [11] Q. Wang, X. Zhang, W. Zhang, and *et al.*, “Realistic lung nodule synthesis with multi-target co-guided adversarial mechanism,” *IEEE T MED IMAGING*, 2021.
- [12] Z. Xu, X. Wang, H. Shin, and *et al.*, “Tunable ct lung nodule synthesis conditioned on background image and semantic features,” in *Proc. MICCAI Workshops SASHIMI*. Springer, 2019, pp. 62–70.
- [13] S. Wang, M. Zhou, Z. Liu, and *et al.*, “Central focused convolutional neural networks: Developing a data-driven model for lung nodule segmentation,” *MED IMAGE ANAL*, vol. 40, pp. 172–183, 2017.
- [14] H. Cao, H. Liu, E. Song, and *et al.*, “Dual-branch residual network for lung nodule segmentation,” *Applied Soft Computing*, vol. 86, p. 105934, 2020.
- [15] P. Isola, J. Zhu, and T. Zhou, “Image-to-image translation with conditional adversarial networks,” in *Proc. IEEE CVPR*, 2017, pp. 1125–1134.
- [16] M. Mirza and S. Osindero, “Conditional generative adversarial nets,” 2014.
- [17] Q. Wang, X. Zhang, W. Chen, and *et al.*, “Class-aware multi-window adversarial lung nodule synthesis conditioned on semantic features,” in *Proc. MICCAI*. Springer, 2020, pp. 589–598.
- [18] S. Gu, J. Bao, H. Yang, and *et al.*, “Mask-guided portrait editing with conditional gans,” in *Proc. IEEE CVPR*, 2019, pp. 3436–3445.
- [19] J. Hu, L. Shen, S. Albanie, and *et al.*, “Squeeze-and-excitation networks,” *IEEE T PATTERN ANAL*, vol. PP, no. 99, 2017.
- [20] N. Otsu, “A threshold selection method from gray-level histograms,” *IEEE T SYST MAN CY-S*, vol. 9, no. 1, pp. 62–66, 2007.
- [21] A. Paszke, S. Gross, F. Massa, and *et al.*, “Pytorch: An imperative style, high-performance deep learning library,” *arXiv preprint arXiv:1912.01703*, 2019.
- [22] M. Z. Alom, M. Hasan, C. Yakopcic, and *et al.*, “Recurrent residual convolutional neural network based on u-net (r2u-net) for medical image segmentation,” 2018.
- [23] B. Toloooshams, R. Giri, A. Song, and *et al.*, “Channel-attention dense u-net for multichannel speech enhancement,” in *Proc. ICASSP*, 2020, pp. 836–840.
- [24] P. Amorim, T. F. Moraes, J. Silva, and *et al.*, “Lung nodule segmentation based on convolutional neural networks using multi-orientation and patchwise mechanisms,” in *Proc. VipIMAGE*, 2019, pp. 286–295.
- [25] A. A. Farag, H. Munim, and J. H. Graham, “A novel approach for lung nodules segmentation in chest ct using level sets,” *IEEE T IMAGE PROCESS*, vol. 22, no. 12, pp. 5202–5213, 2013.
- [26] F. Milletari, N. Navab, and S. Ahmadi, “V-net: Fully convolutional neural networks for volumetric medical image segmentation,” in *Proc. 3DV*, 2016, pp. 565–571.
- [27] S. Ji, W. Xu, M. Yang, and *et al.*, “3d convolutional neural networks for human action recognition,” *IEEE T PATTERN ANAL*, vol. 35, no. 1, pp. 221–231, 2013.
- [28] Z. Zhou, R. Siddiquee, M. Mahfuzur, and *et al.*, “Unet++: A nested u-net architecture for medical image segmentation,” in *Proc. DLIA Workshop*, 2018, pp. 3–11.
- [29] O. Ronneberger, P. Fischer, and T. Brox, “U-net: Convolutional networks for biomedical image segmentation,” in *Proc. MICCAI*. Springer, 2015, pp. 234–241.
- [30] S. F. Huang, R. Chang, D. Chen, and *et al.*, “Characterization of spiculation on ultrasound lesions,” *IEEE T MED IMAGING*, vol. 23, no. 1, pp. 111–121, 2004.